

Ultrafast non-volatile rewritable ferroaxial switching

Z. Zeng^{1,2}, M. Först¹, M. Fechner¹, D. Prabhakaran², P. G. Radaelli², A. Cavalleri^{1,2}

¹*Max Planck Institute for the Structure and Dynamics of Matter, Hamburg, Germany*

²*Department of Physics, Clarendon Laboratory, University of Oxford, Oxford, United Kingdom*

Ultrafast switching of ferroic phases is an important research frontier, with significant technological potential. Yet, current efforts are meeting some key challenges, ranging from limited speeds in ferromagnets to intrinsic volatility of switched domains due to uncompensated depolarizing fields in ferroelectrics. Unlike these ferroic systems, ferroaxial materials host bistable states that do not break spatial-inversion or time-reversal symmetry, and are therefore immune to depolarizing fields. Yet, they are difficult to manipulate because external axial fields are not easily constructed with conventional methods. Here, we demonstrate ultrafast switching of ferroaxial order by engineering an effective axial field made up of circularly driven terahertz phonon modes. A switched ferroaxial domain remains stable for many hours and can be reversed back with a second terahertz pulse of opposite helicity. The effects demonstrated here may lead to a new platform for ultrafast information storage.

Ferroic orders in solids exhibit pairs of energetically degenerate macroscopic states that can be switched by the application of a corresponding conjugate field. Well-known examples of ferroic order are ferromagnetism and ferroelectricity, which break time reversal and spatial inversion symmetry, respectively, and are used in memories, sensors, actuators and spintronic devices(1, 2). Ferroaxial order is a distinct type of ferroic order, characterized by a rotational texture that hosts vortices of electric dipoles. Ferroaxial order does not break either spatial inversion or time reversal symmetry (3-6). Because, no net polarization nor net magnetization are present, ferroaxials are free from depolarizing or stray fields (7, 8), making them promising candidates for stable, non-volatile data storage. Furthermore, ferroaxial order provides a symmetry channel that mediates the coupling between chiral magnetic textures and electric polarizations (9-12), and is of interest to research in

multiferroics. These unique functional properties have driven rapid advances in both the exploration of new ferroaxial materials (13-18) and the development of new techniques for probing their domain structures (19-22).

Rubidium iron dimolybdate, $\text{RbFe}(\text{MoO}_4)_2$, is a prototypical ferroaxial system with a transition temperature T_c of about 190K(23-26). Above T_c , the material crystallizes in a high-symmetry para-axial state of space group $P\bar{3}m1$. Cooling through the transition temperature spontaneously breaks multiple mirror symmetries, lowering the crystal symmetry to $P\bar{3}$. The spontaneous symmetry breaking in $\text{RbFe}(\text{MoO}_4)_2$ results in two opposite ferroaxial domains, A+ and A-, corresponding to clockwise and counterclockwise rotations of the FeO_6 octahedra, respectively (Fig. 1a).

This type of symmetry breaking is invisible to linear optical probes, but gives rise to a circular dichroism in electric quadrupole second-harmonic generation (SHG-CD)(27, 28), providing a sensitive measure of the ferroaxial domain state(21). The emergence of ferroaxial order in $\text{RbFe}(\text{MoO}_4)_2$ is evidenced by temperature-dependent SHG-CD, which displays a sharp increase to a finite value at T_c (Fig. 1b). Notably, the SHG-CD is either positive or negative for the two ferroaxial domains(21), enabling direct optical identification of their orientation (see Supplementary Information). Spatial mapping resolves the multi-domain structure below T_c , with domain sizes of about 100 micrometers (inset of Fig. 1b)(20).

Ferroaxial conjugate field engineering

The ferroaxial order parameter is a time-reversal invariant axial vector(4), defined as $\vec{A} = \vec{r} \times \vec{P}$, the cross product of the position vector \vec{r} and the local electric dipole moment \vec{P} . Direct external control of this order requires a conjugate field that transforms in the same way as the order parameter under all symmetry operations of the system(29). This can be realized by the cross product of two different polar fields, $\vec{X} \times \vec{Y}$, applied simultaneously along two different directions(29-32). However, combining conventional fields such as electric fields \vec{E} , thermal gradients ∇T or longitudinal strain gradients $\partial_i \varepsilon_{ii}$ in a well-controlled configuration is experimentally challenging(33, 34).

We construct a ferroaxial conjugate field $\vec{F} = \vec{Q} \times \vec{E}$ by a terahertz (THz) light field \vec{E} and the displacement \vec{Q} of an infrared-active phonon resonantly driven by this field(35-48). Linearly polarized THz pulses, which are commonly used to excite atomic motions parallel to the THz electric field(41, 43, 49), do not couple to the ferroaxial order, because the field $\vec{F} = \vec{Q} \times \vec{E}$ vanishes. On the other hand, circularly polarized THz pulses drive circular atomic motions when resonantly exciting a pair of degenerate phonon modes(50-56). In this dynamical setting, both the electric field and the phonon displacement rotate continuously, while the cross product of the two fields $\vec{F} = \vec{Q} \times \vec{E}$ remains directionally fixed (Fig. 2a). This configuration offers an experimentally accessible conjugate field to ferroaxial order (57), which can be reversed depending on the helicity of the THz electric field.

In $\text{RbFe}(\text{MoO}_4)_2$, the ferroaxial order develops along the crystal c axis and is characterized by the axial mode Q_A subject to a temperature-dependent potential $U(Q_A, T)$. Dynamically, the axial mode couples to the z -component of the conjugate field $(\vec{Q} \times \vec{E})_z$ via the interaction potential $\Delta U = \alpha(\vec{Q} \times \vec{E})_z Q_A$. Below T_c , the potential $U(Q_A, T)$ takes the form of a symmetric double-well, with each well corresponding to one of the two ferroaxial domains. A circular phonon excitation lifts the degeneracy between the two domains by lowering the energy of one well relative to the other (Fig. 2b). Above T_c , $\text{RbFe}(\text{MoO}_4)_2$ is in a para-axial state with a single-well potential. Here, a circular phonon excitation shifts the minimum of the well, transiently inducing as an *axially polarized state* (Fig. 2c). In both cases, the direction of the torque applied on the ferroaxial soft mode is controlled by the helicity of the THz excitation pulse.

Single-shot switching of ferroaxial order below T_c

As illustrated in Figure 3a, ferroaxial switching by the THz pulse below T_c is expected due to the transient asymmetric lowering of the double-well potential. This process is captured by the following equations of motion:

$$\frac{\partial^2}{\partial t^2} \vec{Q}_{E_u} + \gamma_{E_u} \frac{\partial}{\partial t} \vec{Q}_{E_u} + \omega_{E_u}^2 \vec{Q}_{E_u} = Z_{E_u}^* \vec{E}(t) \quad (1)$$

$$\frac{\partial^2}{\partial t^2} Q_A + \gamma_A \frac{\partial}{\partial t} Q_A + \frac{\partial}{\partial Q_A} U(Q_A) = \alpha (\vec{Q}_{E_u}(t) \times \vec{E}(t))_z \quad (2)$$

Here, γ_A and γ_{E_u} are the damping coefficients, ω_{E_u} the frequency of the driven phonon modes. $Z_{E_u}^*$ is the effective charge that couples the in-plane phonon displacement vector \vec{Q}_{E_u} to the pulsed THz electric field $\vec{E}(t) = E_0 \begin{pmatrix} \cos(\omega_{E_u} t) \\ \cos(\omega_{E_u} t + \phi) \end{pmatrix} e^{-\frac{t^2}{2\tau^2}}$, where $\phi = \pm \frac{\pi}{2}$ correspond to left-circular and right circular polarization, respectively. Numerical solutions of these equations reveal the evolution of the ferroaxial order as a function of the THz pulse excitation fluence, showing that a single pulse induces a reversal of the order parameter above a switching threshold (Fig. 3b), which is analogous to the coercive field of a ferroelectric. Similar switching behavior is obtained when starting in the opposite domain by changing the helicity of the THz excitation pulse (see Supplementary Information).

We validated this approach using the optical setup illustrated in Figure 4a. We excited the doubly degenerate E_u -symmetry phonon at 24 THz frequency in the ab -plane of $\text{RbFe}(\text{MoO}_4)_2$ with resonant, circularly polarized THz pulses, and probed the ferroaxial state with SHG-CD measurements (see Supplementary Information). First, we applied a single right-circularly polarized THz pulse with a fluence of 20 mJ/cm^2 at normal incidence to an A+ domain at 180 K lattice temperature (below T_c), identified by its positive static SHG-CD. Following this single-pulse excitation, the static SHG-CD at the excited sample spot was measured again and showed a negative static SHG-CD of approximately same magnitude, indicating that the A+ state was locally switched to an A- state (Fig. 4b). In a second step, a single left-circularly polarized THz pulse, with the same fluence but opposite helicity, illuminated the

same spot. Following this second pulse, the static SHG-CD reverted to a positive value, evidencing that the system switched back to the A+ state.

A sequence of THz pulses with alternating helicities was then applied to the same sample spot, with static SHG-CD measurements performed between pulses to monitor the ferroaxial state. The signal was observed to alternate between positive and negative values, demonstrating reversible optical switching between A+ and A- ferroaxial states (Fig. 4b).

We investigated the fluence dependence of the ferroaxial state switching, aiming to map a ‘hysteresis loop’ of the ferroaxial order under circular phonon excitation. The experiment was performed with single, right-circularly polarized THz pulses of increasing fluence, with static SHG-CD measured for about 20 minutes after each excitation pulse. As shown in Figure 5a, single THz pulses up to an excitation fluence of 12.5 mJ/cm^2 left the A+ ferroaxial state unaffected with a positive static SHG-CD. A subsequent THz pulse with a fluence of 14 mJ/cm^2 inverted the static SHG-CD signal to a negative value, evidencing the ferroaxial state switching above this threshold. On the same sample spot, now in the A- ferroaxial state, this protocol was repeated using left-circularly polarized THz pulses, i.e. of opposite helicity. The SHG-CD signal returned to a positive value, characteristic of the A+ state, at the same excitation fluence of 14 mJ/cm^2 (Fig. 5b). The observed threshold behavior is in qualitative agreement with the predictions from the equations of motion in our circular phonon excitation model (Fig. 3b).

Notably, the rewritable domain was found to be virtually non-volatile, remaining in the switched state for more than six hours – the duration between switching from A+ state to A- state and back to the A+ state in the measurement shown Fig. 5b.

Polarizing the para-axial state above T_c

We further explored the possibility of using circular phonon excitation to induce a transient axial polarization in para-axial $\text{RbFe}(\text{MoO}_4)_2$ above T_c . A left-circularly polarized THz pulse centered at 24 THz, as above in resonance with the in-plane infrared-active E_u -symmetry phonons, is expected to

transiently shift the single-well potential of the para-axial state, centered at $Q_A = 0$, to an A+ axial state (Fig. 6a). Conversely, a transient A- axial state is expected for excitation with a right-circularly polarized THz pulse.

Figure 6b shows the time-resolved SHG-CD induced by excitation with a 600-femtosecond, left-circularly polarized THz pulse at a fluence of 6 mJ/cm^2 at 200 K (above T_C). The short-lived, positive SHG-CD signal refers to the emergence of a transient A+ axial polarization. Its lifetime suggests that the duration of the axial conjugate field is determined by the temporal overlap between the THz pulse and the resonantly driven phonon. Excitation with a right-circularly polarized THz pulse induced a short-lived negative SHG-CD signal (Fig. 6c), evidencing a transient A- axial polarization. The helicity-dependent response above T_C is consistent with a model in which circular phonon excitation serves as the conjugate field for axial order. Excitation linearly polarized THz pulses, did not show detectable SHG-CD, confirming that the conjugate field requires circularly polarized excitation (see Supplementary Information).

The temperature dependence of the photo-induced axial state above T_C is shown in Fig. 6d. The amplitude of the transient SHG-CD signal, measured under left-circularly polarized excitation at a fixed fluence of 6 mJ/cm^2 , increases as the sample temperature approaches T_C . This response of the axial order parameter is characteristic of ferroic systems, which exhibit increased susceptibility near phase transitions(58, 59).

The frequency dependence of the photo-induced axial state as a function of the center frequency of the THz excitation pulses, measured at 200K and a constant excitation fluence of 6 mJ/cm^2 , is shown in Fig. 6e. We found a resonant enhancement in the transient SHG-CD response at the 24-THz frequency of the doubly degenerate in-plane E_u -symmetry phonon mode, which verifies the essential role of resonant phonon excitation when inducing the axial order by light (see Supplementary Information).

Discussion and conclusion

We experimentally demonstrated the generation of a conjugate field for ferroaxial order(31) in the prototypical ferroaxial system $\text{RbFe}(\text{MoO}_4)_2$. This protocol is expected to be broadly applicable across a wide range of ferroaxial materials(31, 60-62). Switching the ferroaxial order represents a distinct advantage over earlier attempts to reverse ferroelectric polarization in LiNbO_3 with light, where excitation of an auxiliary high-frequency infrared-active mode was nonlinearly coupled to the ferroelectric soft mode(38, 63). In that case, a complete reversal of the ferroelectric polarization was inhibited, likely due to the buildup of a depolarizing field at the driven region, which destabilized the switched state(64). The control of the ferroaxial state (65) opens opportunities for applications in data storage and next-generation electronic and magnetic devices(62, 66, 67), flanking the field of optically controlled ferro- and ferrimagnetic order(68-74). Moreover, the emergence of axially in the para-axial state above the critical temperature highlights the strength of coherent electromagnetic fields to engineer functionality of complex materials that do not have equilibrium counterparts.

Figures:

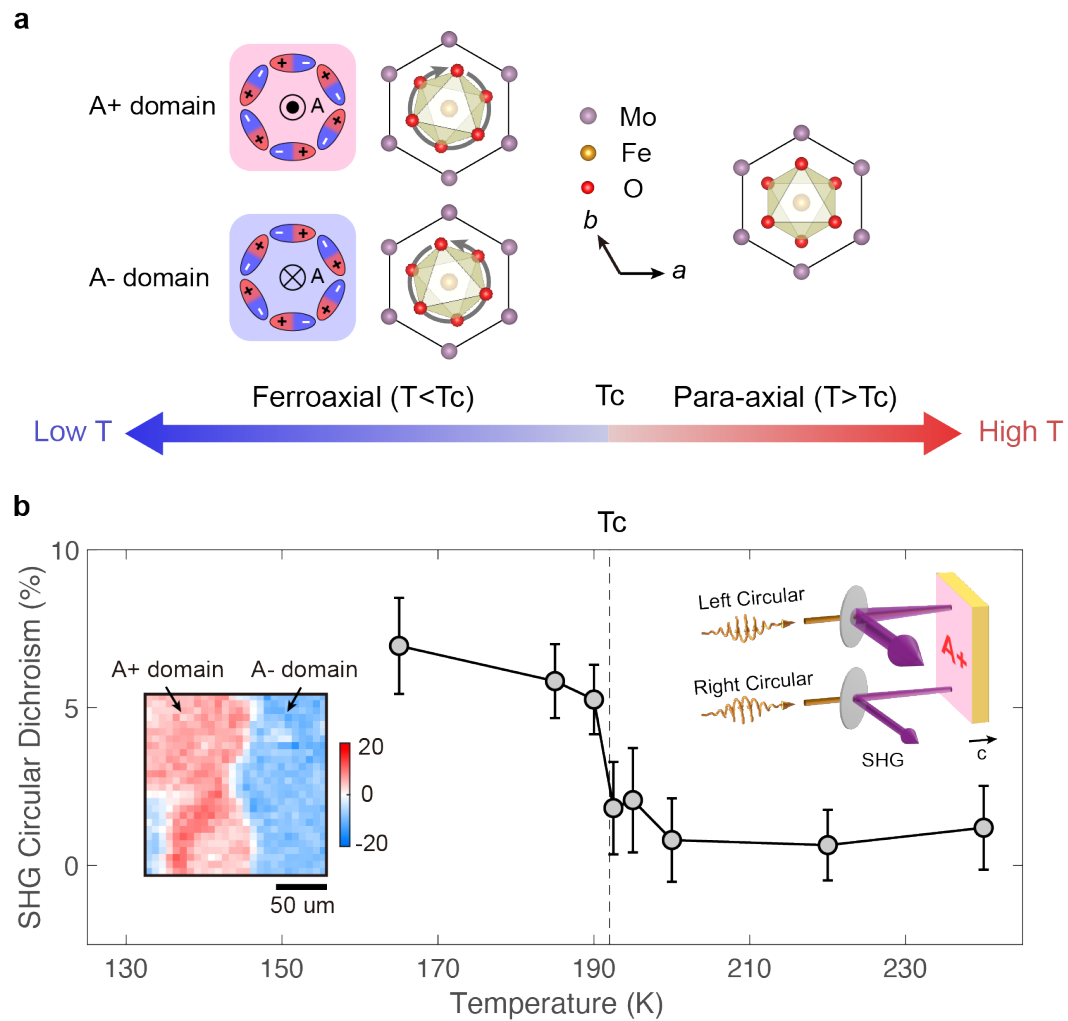


Fig. 1 | Ferroaxial order in $\text{RbFe}(\text{MoO}_4)_2$. **a**, Crystal structure of $\text{RbFe}(\text{MoO}_4)_2$ viewed along the crystal c axis, above and below the structural phase transition temperature T_c . Below T_c , two ferroaxial domains exist (A+ and A-), corresponding to clockwise and counterclockwise rotations of the FeO_6 octahedra, respectively. **b**, Ferroaxial transition characterized by second-harmonic generation circular dichroism (SHG-CD). Error bars denote the standard error of the mean. Right inset: schematic of the SHG-CD measurement. In the A+ ferroaxial domain, the SHG intensity is higher for the left-circularly polarized probe than for the right-circularly polarized probe. Left inset: SHG-CD domain mapping at 170K (below T_c).

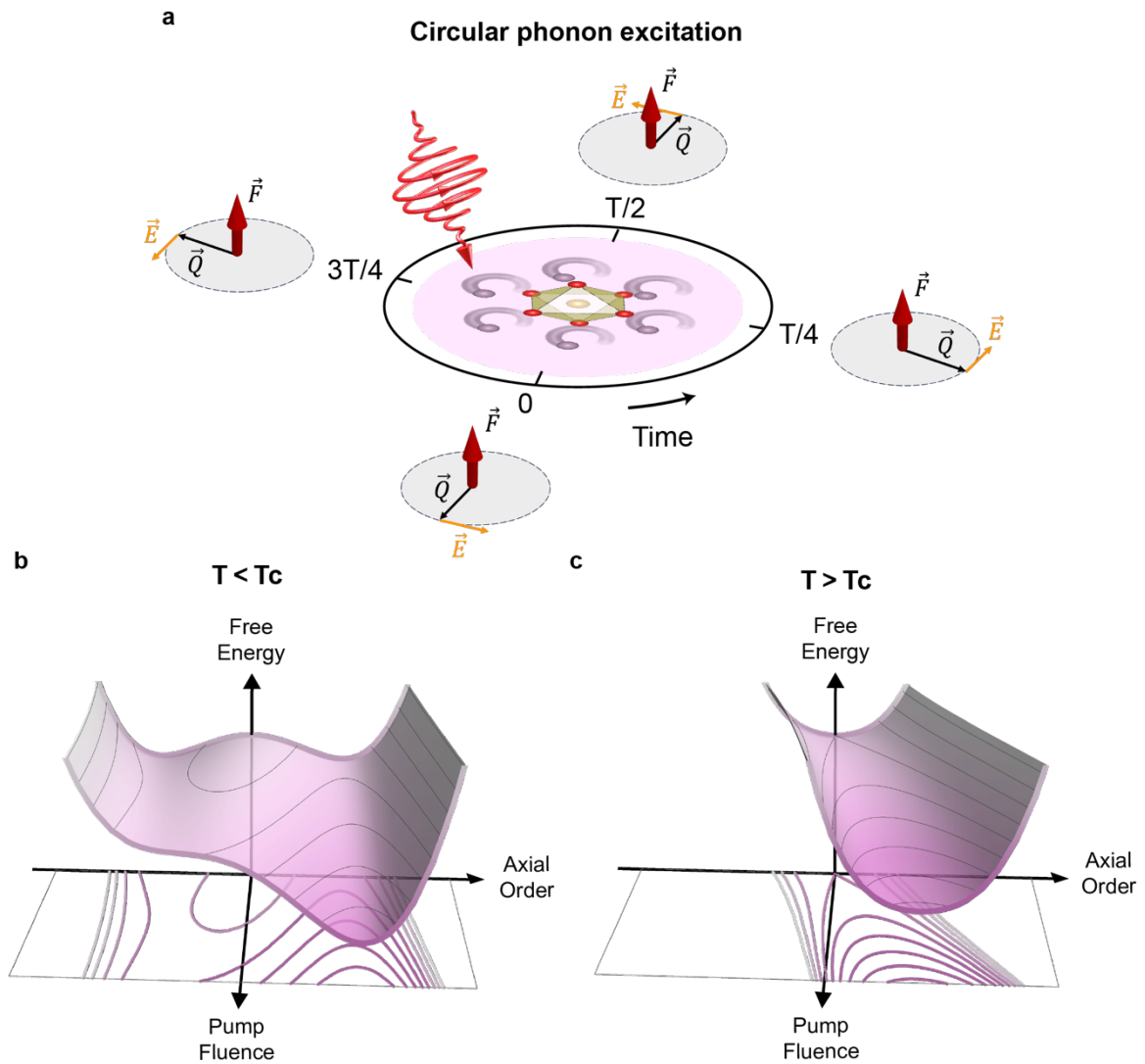


Fig. 2 | Circular phonon excitation as a conjugate field of axial order. **a**, A circularly polarized THz pulse, resonant with a doubly degenerate infrared-active phonon, excites circular phonon motion. At each moment during the drive, the electric field \vec{E} and the phonon displacement \vec{Q} are orthogonal, and the direction of the cross product of $\vec{E} \times \vec{Q}$ remains fixed. **b**, Potential energy landscape of axial order under circular pump below T_c . A circularly polarized THz pump biases the double-well potential, favoring one domain over the other, as shown here for a left-circularly polarized THz pulse. **c**, Potential energy landscape of axial order under circular pump in the para-axial state above T_c . A circularly polarized pump shifts the potential energy minimum from zero to a finite value of the axial order parameter, shown here again for a left-circularly polarized THz pulse.

Single-shot switching below T_c

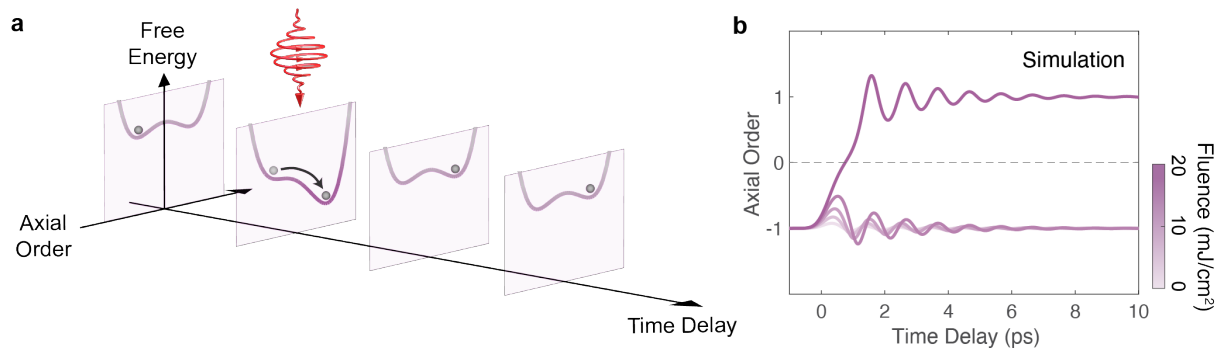


Fig. 3 | Simulation of single-shot switching of ferroaxial order. a, Schematic potential energy landscape snapshots of the axial order for circularly polarized phonon excitation below T_c . The circularly polarized pump biases the double-well potential and switches the ferroaxial domain. **b,** Dynamics of the axial order for this excitation at various fluences below and above threshold.

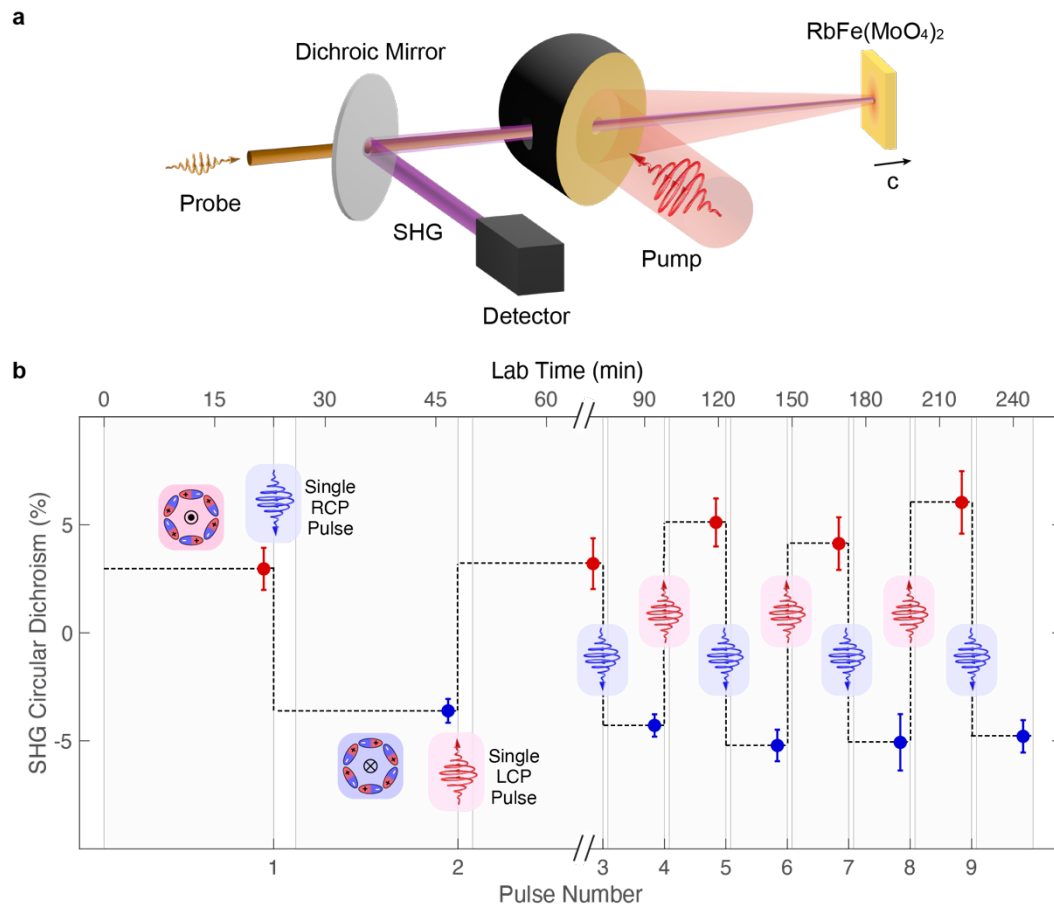


Fig. 4 | Demonstration of single-shot switching of ferroaxial order below T_c . **a**, Schematic of the experimental setup. A circularly polarized THz excitation pulse, polarized in the ab -plane, drives circular motion of the doubly degenerate E_u symmetry phonons in $\text{RbFe}(\text{MoO}_4)_2$. SHG-CD monitors the ferroaxial state at the excited position. **b**, Measurement of the ferroaxial domain state between single THz excitation pulses. The SHG-CD measurement averages over the shaded time windows. Error bars denote the standard error of the mean.

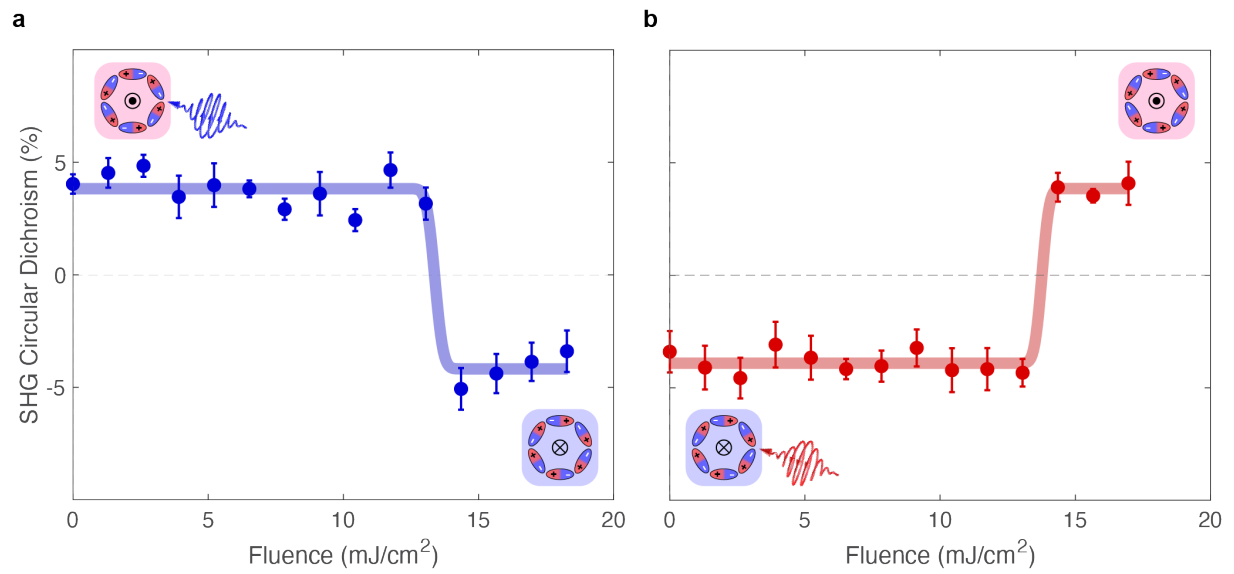


Fig. 5 | Fluence-dependent single-shot switching of the ferroaxial order. a, Measurement of the SHG-CD, probing the ferroaxial order after each of the single, right-circularly polarized THz excitation pulses of increasing fluence. **b,** Same measurement for left-circularly polarized single-shot pump pulses. Error bars denote the standard error of the mean.

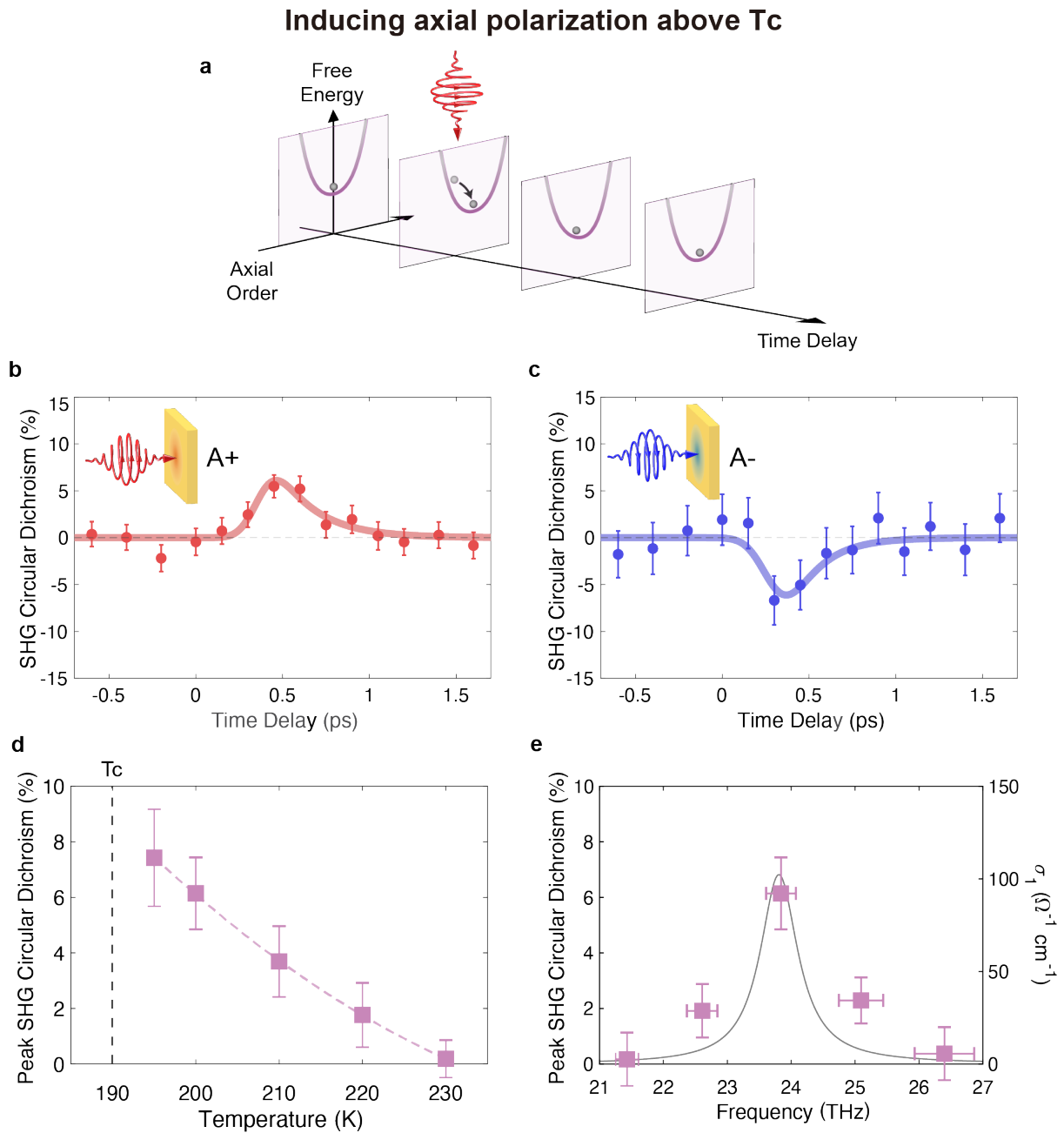


Fig. 6 | Photo-induced axial order in the para-axial state above T_c . **a**, Schematic potential energy landscape snapshots of the axial order for a circularly polarized THz excitation pulse above T_c , shifting the potential energy minimum. **b**, Time delay dependent SHG-CD measurement for right-circularly polarized excitation. **c**, Time delay dependent SHG-CD measurement for left-circularly polarized excitation. **d**, Peak amplitude of the transient SHG-CD response as a function of temperature above T_c . **e**, Peak amplitude of the transient SHG-CD response as a function of the center frequency of the excitation pulse. The gray curve corresponds to the real part of the optical conductivity. Vertical error bars denote the standard error of the mean. Horizontal error bars in **e** represent the 1σ confidence interval of the center frequency of the excitation pulses.

Supplementary Materials for

Ultrafast non-volatile rewritable ferroaxial switching

Z. Zeng^{1,2}, M. Först¹, M. Fechner¹, D. Prabhakaran², P. G. Radaelli², A. Cavalleri^{1,2}

¹*Max Planck Institute for the Structure and Dynamics of Matter, Hamburg, Germany*

²*Department of Physics, Clarendon Laboratory, University of Oxford, Oxford, United Kingdom*

S1. Materials and Methods

S2. SHG Circular Dichroism and the Assignment of Ferroaxial Domains

S3. Density Functional Theory Calculations

S5. Simulations of the Axial Order Dynamics

S5. Time-resolved SHG-CD above T_c for Linearly Polarized Excitation

S1. Materials and Methods

S1.1. Experimental Setup

A schematic drawing of the pump-probe setup used in the experiment is shown in Figure S1. The THz pump pulses were generated by difference frequency generation (DFG) in a GaSe crystal⁽⁷⁵⁾, using the independently wavelength-tunable near-infrared signal outputs of two optical parametric amplifiers (OPAs). The OPAs were seeded by the same white light and pumped by overall 11-mJ, 35-fs pulses at 800 nm wavelength from a Ti:sapphire amplifier operating at 1-kHz repetition rate. Following the DFG process, linearly polarized THz pump pulses were temporally stretched to ~600 fs by passing through two 5-mm-thick ZnSe crystals positioned at the Brewster angle. The THz spectrum was characterized by Fourier transform infrared spectroscopy (Fig. S2a).

A CdSe-based infrared quarter waveplate induced circular polarization of the THz pulses, which was characterized by detecting the optical power transmitted through a rotating linear polarizer (Fig. S2b). A combination of two free-standing wire grid polarizers before the quarter waveplate allowed us to reverse the helicity of the THz excitation pulses between left- and right-circularity and control the excitation fluence without rotating the quarter waveplate. This approach ensured the identical alignment and spot position on the sample for both helicities. An off-axis parabolic mirror was then used to focus the THz beam onto the sample with a ~70 μm spot size (full width at half maximum intensity, FWHM).

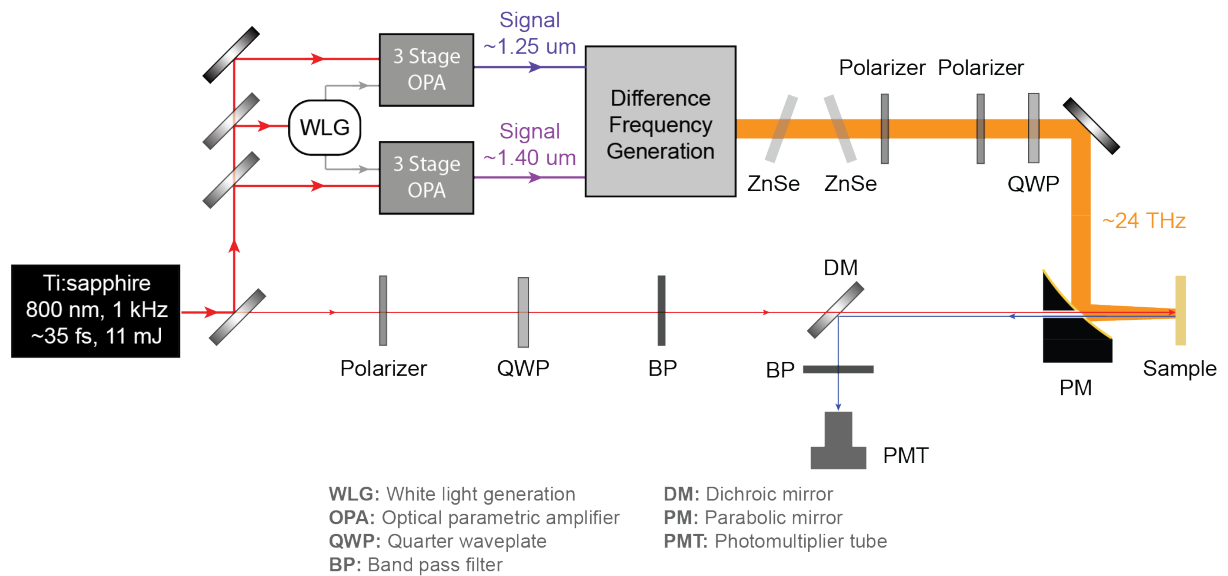


Figure S2. | Schematic of the experimental setup.

The probe pulses for the measurement of the second-harmonic generation circular dichroism (SHG-CD) were sourced by the same amplifier system and focused with a lens onto the sample to a spot size of $\sim 30 \mu\text{m}$ (FWHM). Circular polarization of the probe incident on the sample was achieved using another quarter waveplate. The SHG-CD signals were measured in reflection geometry with a coherence length in the SHG process of about 50 nm,⁽⁷⁶⁾ shorter than the 500-nm extinction depth of the THz pulses at the phonon resonance. A pair of narrow bandpass filters was employed before and after the sample to filter out side-band components in the pump-probe measurements arising from electric-field-induced second-harmonic generation (EFISH) effect. The filter before the sample transmits at 808 nm center wavelength, with a 5-nm bandwidth, whilst the filter on the SHG output is centered at 404 nm with a bandwidth of 2 nm.

The pump and probe beams were aligned collinearly and at normal incidence to the sample surface of c-cut $\text{RbFe}(\text{MoO}_4)_2$, in this way preserving the circular polarization in the excitation and detection processes. All measurements were performed in an optical cryostat under vacuum conditions ($< 10^{-6}$ mbar).

For the preparation of single THz excitation pulses, two optical choppers with 10% duty cycle, synchronized to the Ti:sapphire amplifier system, were placed in the THz beam path before the sample,

reducing the repetition rate from 1 kHz to 10 Hz. A synchronized fast shutter was then used to select single pulses for the optical excitation.

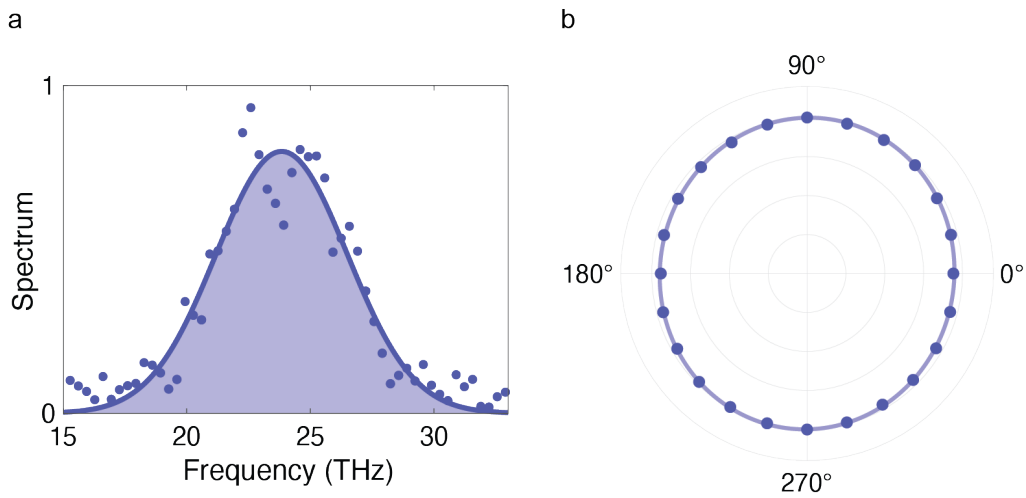


Figure S2. | Characterization of the THz excitation pulses. (a) Frequency spectrum of the excitation pulse, centered at 24 THz, characterized by Fourier transform infrared spectroscopy. (b) Measurement of the polarization state of the left-circularly polarized 24-THz excitation pulses, showing a 97% ellipticity.

S1.2. Sample Preparation and Characterization

Single crystal $\text{RbFe}(\text{MoO}_4)_2$ was grown using the flux method and characterized by x-ray diffractometry. A sample with an optically flat c-cut surface and thickness of $\sim 200 \mu\text{m}$ was used in this experiment. In the experiments, it was cooled and heated with a slow rate of 0.1 K/min near the 190-K critical temperature.

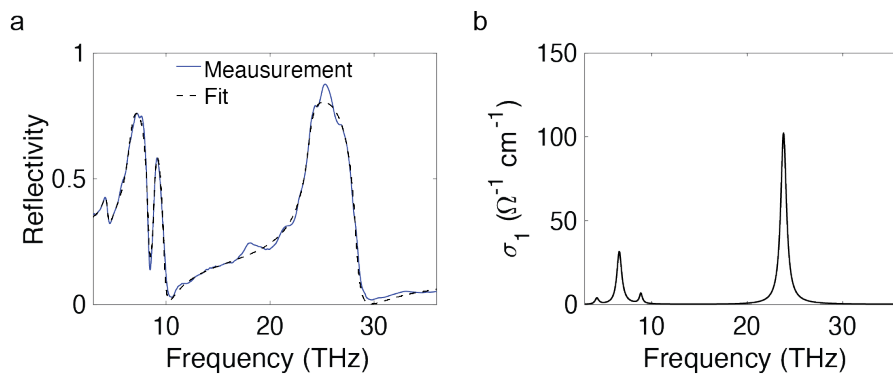


Figure S3. | Static optical characterization of the RbFe(MoO₄)₂ sample. (a) Measured reflectivity spectrum in the THz range with the electric field polarized in the crystal *ab*-plane, along with the corresponding fit. (b) Frequency dependent real part of the optical conductivity extracted from the fit.

The static optical properties in the THz frequency range were characterized by Fourier-transform infrared reflectivity (FTIR) measurements, with the light electric field polarized in the crystal *ab*-plane. As shown in Figure S3, four E_u-symmetry optical phonon modes of RbFe(MoO₄)₂ were found in the reflectivity spectrum, which was fitted using the following dielectric function for infrared-active phonons(77)

$$\varepsilon(\omega) = \varepsilon_{\infty} + \varepsilon_{\infty} \sum_j \frac{\omega_{LO,j}^2 - \omega_{TO,j}^2}{\omega_{TO,j}^2 - \omega^2 - i\omega\gamma_j}$$

The fitting results are summarized in Table S1. In the experiments reported here, we resonantly excited the E_u(4) mode at 24 THz.

Phonon Mode	$\omega_{TO,j}$ (THz)	$\omega_{LO,j}$ (THz)	γ_j (THz)	ε_{∞}
E _u (1)	4.3	4.8	0.45	/
E _u (2)	6.6	9.9	0.61	/
E _u (3)	8.9	9.2	0.38	/
E _u (4)	23.8	27.8	0.72	/
/	/	/	/	4.01

Table S1. | Results of fitting the infrared reflectivity spectrum, polarized in the *ab* plane, by the E_u-symmetry phonon modes in RbFe(MoO₄)₂.

S2. SHG Circular Dichroism and the Assignment of Ferroaxial Domains

RbFe(MoO₄)₂ crystallizes in a centrosymmetric structure both above and below T_c. Since electric dipole SHG signal is forbidden, the observed SHG signal arises from higher-order processes, predominantly electric quadrupole SHG(25).

The SHG Circular Dichroism (SHG-CD) signal in this study is defined as the normalized difference of the SHG intensity detected between left-circularly polarized (LCP) and right-circularly polarized (RCP) normal-incident near-infrared probe pulses.

$$SHG-CD = \frac{I_{LCP} - I_{RCP}}{I_{LCP} + I_{RCP}}$$

Based on symmetry analysis, the SHG-CD signal is expected to be zero in the para-axial state and finite in the ferroaxial state, with opposite signs for opposite ferroaxial domains(21).

The exact correspondence between the sign of the SHG-CD signal and the ferroaxial domain state is unknown and not easily accessible through static characterization. For the convenience of analysis and discussion, we assigned domains with a positive SHG-CD signal as A+ domains and those with a negative SHG-CD signal as A- domains. The validity of this assignment is supported by the helicity-dependent response induced by the circular THz excitation, which agrees in sign with theoretical calculations(57).

S3. Density Functional Theory Calculations

We carried out first-principles calculations based on density functional theory (DFT+U) to investigate the phonon excitation spectrum, anharmonic lattice interactions, and optical properties of RbFe(MoO₄)₂. All simulations were conducted using the Vienna Ab-initio Simulation Package (VASP, version 6.5.1)(78-80), with phonon-related calculations carried out via the Phonopy package(81).

Pseudopotentials were used within the Projector Augmented Wave (PAW) framework(82), employing standard potentials for Rb (4p⁶5s¹), Fe (3p⁶3d⁶4s²), Mo (4d⁵5s¹), and O (2s²2p⁴). The Local Density Approximation (LDA) was chosen for the exchange-correlation functional, augmented by the Hubbard *U-J* correction to account for the localized d-electrons of Fe.

Consistent with a previous study(57), we found that the phonon and related properties are insensitive to the precise value of U , and thus adopted $U = 4$ eV and $J = 0$ eV.

After convergence testing, structural relaxation and phonon calculations were performed using a $7 \times 7 \times 5$ Monkhorst-Pack k-point grid(83) and a plane-wave cutoff energy of 600 eV. Self-consistent iterations continued until total energy changes fell below 10^{-8} eV. All phonon and anharmonic coupling constant evaluations were carried out in the primitive unit-cell of $\text{RbFe}(\text{MoO}_4)_2$.

Our starting point was the $P\bar{3}m1$ high-temperature crystal structure of $\text{RbFe}(\text{MoO}_4)_2$, which we fully structurally relaxed. The resulting lattice parameters are listed in Table S2. Phonon calculations for this structure revealed an unstable A_{2g} ferroaxial soft mode with an imaginary frequency. The frequency of the driven doubly degenerate E_u phonon mode is also reported in Table S2.

To explore the ferroaxial low-temperature phase, we applied a frozen-phonon approach by displacing the structure along the unstable A_{2g} mode. This resulted in the double-well potential shown in Figure S4, indicating a structural instability toward a lower-symmetry $P\bar{3}$ ground state.

Physical Properties	Parameter/Site	a (Å) / x	b (Å) / y	c (Å) / z	Frequency (THz)
Lattice constants	/	5.65	5.65	7.20	/
	Rb	0	0	1/2	/
	Fe	0	0	0	/
Structural coordinates	2Mo	1/3	2/3	0.240	/
	2Oa	1/3	2/3	0.482	/
	6Op	0.160	0.840	0.162	/
Phonon	$E_u(4)$	/	/	/	24.42

Table S2. | Relaxed lattice parameters and selected phonon mode frequency of high-symmetry $\text{RbFe}(\text{MoO}_4)_2$.

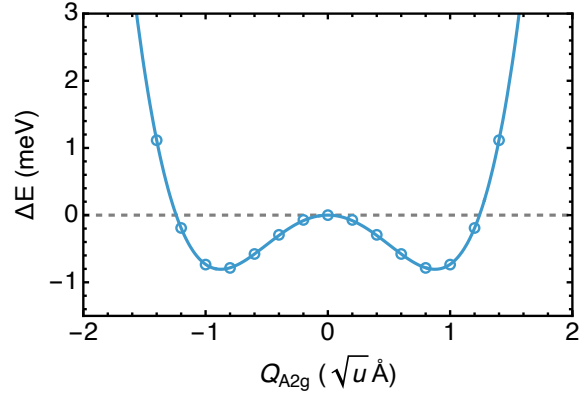


Fig S4. | Double-well potential energy profile obtained by displacing the high-symmetry $\text{RbFe}(\text{MoO}_4)_2$ structure along the unstable A_{2g} ferroaxial mode. The two minima correspond to symmetry-broken configurations associated with the low-temperature $P\bar{3}$ phase, indicating a structural phase transition driven by the soft mode.

From the relaxed high-temperature structure, we mapped the coupling between the infrared-active mode at 24 THz and the optically silent A_{2g} soft mode. Specifically, we computed the off-diagonal term of the mode effective charge tensor as a function of the A_{2g} displacement, which characterizes the trilinear coupling term $\alpha(\vec{Q} \times \vec{E})_z Q_A$ following the methodology outlined in a previous study(57). The resulting coupling coefficient in our computations is $\alpha = 0.026 \text{ q}_e/\text{u}\text{\AA}$, which results in a tilted energy landscape for axial order under circularly polarized excitation (Fig. S5).

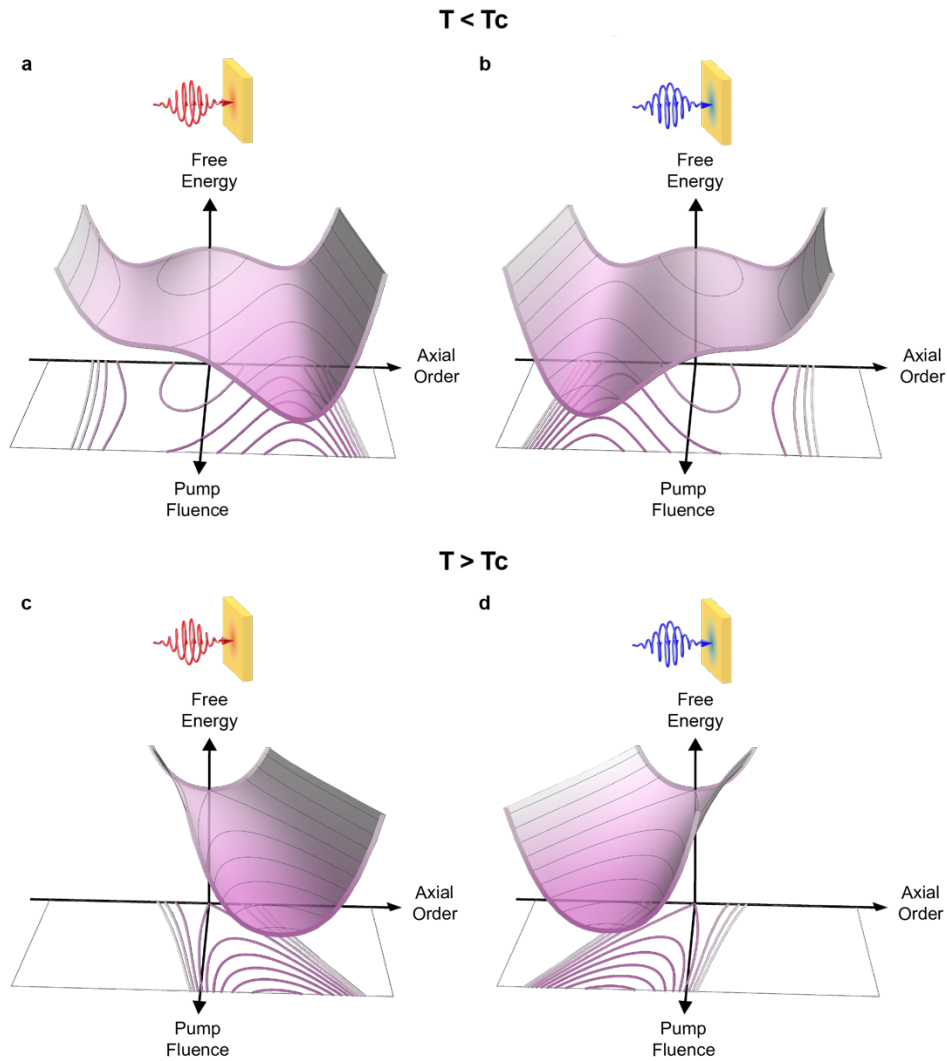


Figure S5. | Schematic potential energy landscape of axial order for circularly polarized THz excitation. (a) Axial order below T_c with left-circularly polarized THz excitation. (b) Axial order below T_c with right-circularly polarized THz excitation. (c) Axial order above T_c with left-circularly polarized THz excitation. (d) Axial order above T_c with right-circularly polarized THz excitation.

S4. Simulations of the Axial Order Dynamics

To model the dynamics of the driven axial state and ferroaxial switching, we solved the equations of motion for the infrared-active mode coupled to the axial soft mode (see main text). We used a circularly-polarized Gaussian pulse that replicates the experimental conditions with a pulse duration of 600 fs (FWHM). To account for finite temperature effects, the harmonic term of the A_{2g} soft mode was scaled using experimentally determined mode frequencies in the low-temperature phase (Fig. S6)(84), following the fitting function

$$\omega^2(T) = \omega_0^2 \left| 1 - \left(\frac{T}{T_C}\right)^\beta \right|$$

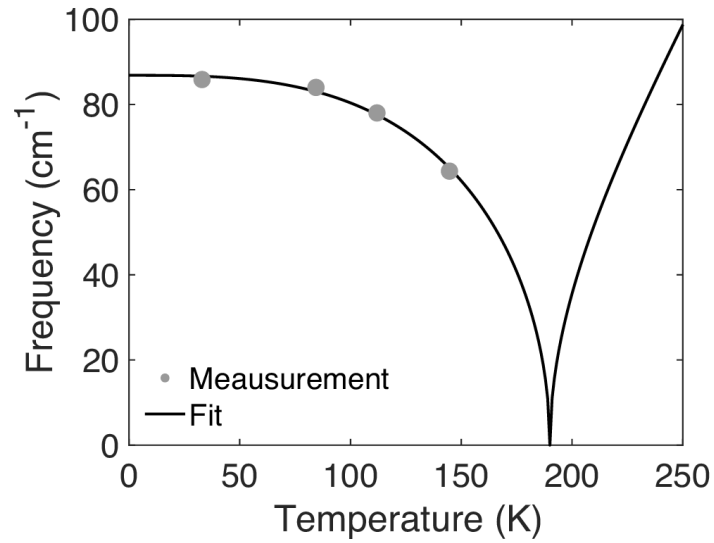


Figure S6. | Experimentally determined axial soft mode frequency (grey dots) and a fit to the data.

The simulated dynamics as a function of fluence below T_C are shown in Figure S7. For the A- ferroaxial initial state, a left-circularly polarized THz excitation pulse above a certain fluence threshold switches the state to the opposite A+ state (Fig. S7a), while the right-circularly polarized excitation leaves it in the A- ferroaxial state (Fig. S7b). Conversely, for the A+ ferroaxial initial state, switching to the A- state is achieved with a right-circularly polarized excitation pulse above the threshold (Fig. S7c), while the left-circularly polarized excitation leaves the A+ state unchanged (Fig. S7d).

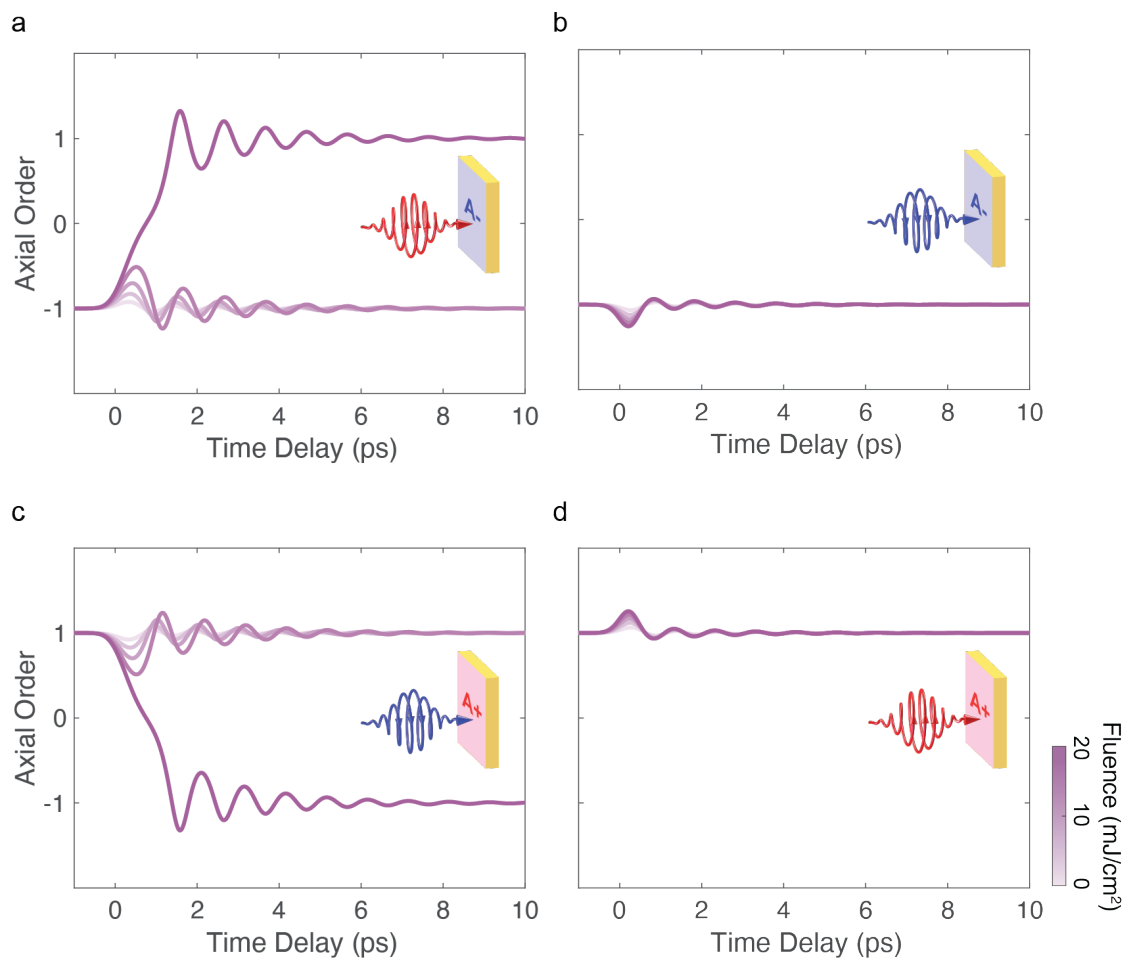


Figure S7. | Calculated dynamics of axial order for circularly polarized excitation at different fluences below T_c . (a) Dynamics of an A- ferroaxial initial state under left-circularly polarized THz excitation. (b) Dynamics of an A- ferroaxial initial state under right-circularly polarized THz excitation. (c) Dynamics of an A+ ferroaxial initial state under right-circularly polarized THz excitation. (d) Dynamics of an A+ ferroaxial initial state under left-circularly polarized THz excitation.

Simulations were also performed above T_c , for a fixed excitation fluence of 6 mJ/cm^2 matching the experimental conditions. A left-circularly polarized pump induces a transient positive axial order (Fig. S8a), while a right-circularly polarized pump induces a transient negative axial order (Fig. S8b). In both cases, the amplitude of the transient order increases as the temperature approaches the ferroaxial transition temperature, reflecting the softening of the axial mode.

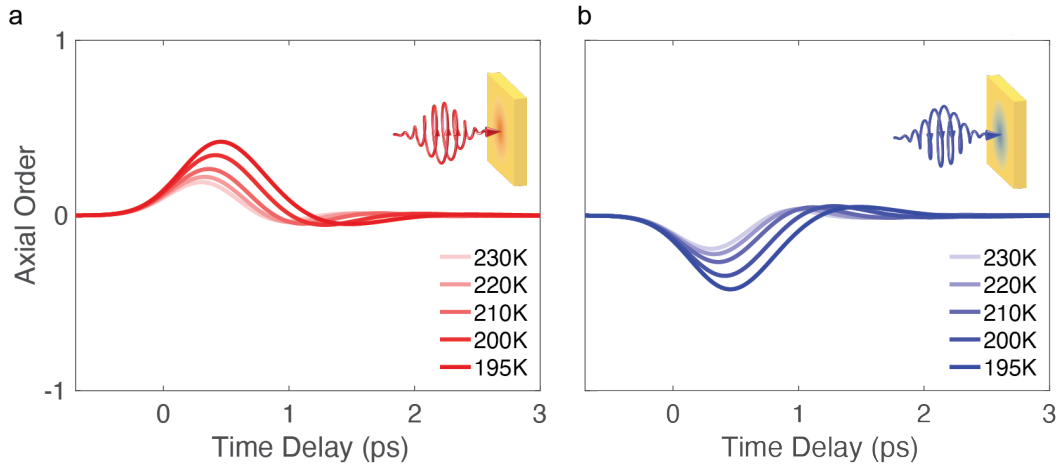


Figure S8. | Calculated dynamics of the axial order for circularly polarized excitation pulses at different temperatures above T_c . (a) Transient A+ axial order induced by a left-circularly polarized THz pulse. (b) Transient A- axial order induced by a right-circularly polarized THz pulse.

S5. Time-resolved SHG-CD above T_c for Linearly Polarized Excitation

Time-resolved SHG-CD measurements of a possible light-induced axial state above T_c were also taken using linearly polarized THz pulses at a fluence of 6 mJ/cm^2 and at 200 K lattice temperature, again with the pump polarization in the crystal ab -plane (perpendicular to the crystal a axis). We did not observe finite transient SHG-CD, strongly suggesting that the conjugate field of the axial order vanishes under linearly polarized excitation, in agreement with the model presented in the main text.

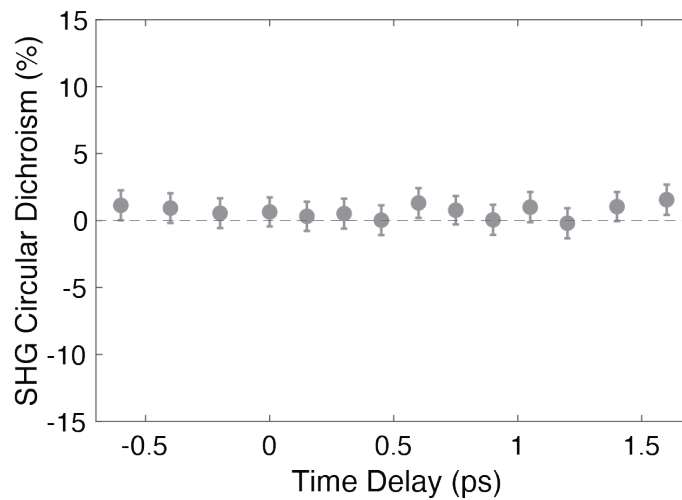


Figure S9. | Time-resolved SHG-CD using linearly polarized THz excitation pulses of 6 mJ/cm^2 fluence at 200 K lattice temperature (above T_c). Error bars denote the standard error of the mean.

References

1. A. MacDonald, r. P. Schiffer, h. N. Samarth, Ferromagnetic semiconductors: moving beyond (ga, mn) as. *Nature materials* **4**, 195-202 (2005).
2. L. W. Martin, A. M. Rappe, Thin-film ferroelectric materials and their applications. *Nature Reviews Materials* **2**, 1-14 (2016).
3. A. Andreev, I. Grishchuk, Spin nematics. *Sov. Phys. JETP* **60**, 267 (1984).
4. V. Dubovik, L. Tosunyan, V. Tugushev, Axial toroidal moments in electrodynamics and solid-state physics. *Zh. Eksp. Teor. Fiz* **90**, 590-605 (1986).
5. J. Hlinka, Eight types of symmetrically distinct vectorlike physical quantities. *Physical Review Letters* **113**, 165502 (2014).
6. S. Bhowal, N. A. Spaldin, Electric toroidal dipole order and hidden spin polarization in ferroaxial materials. *Physical Review Research* **6**, 043141 (2024).
7. M. Dawber, P. Chandra, P. Littlewood, J. Scott, Depolarization corrections to the coercive field in thin-film ferroelectrics. *Journal of Physics: Condensed Matter* **15**, L393 (2003).
8. P. Chandra, M. Dawber, P. Littlewood, J. Scott, Scaling of the coercive field with thickness in thin-film ferroelectrics. *Ferroelectrics* **313**, 7-13 (2004).
9. R. Johnson *et al.*, Cu₃Nb₂O₈: a multiferroic with chiral coupling to the crystal structure. *Physical review letters* **107**, 137205 (2011).
10. R. Johnson, L. Chapon, D. Khalyavin, P. Manuel, P. Radaelli, C. Martin, Giant improper ferroelectricity in the ferroaxial magnet CaMn₇O₁₂. *Physical review letters* **108**, 067201 (2012).
11. A. J. Hearmon *et al.*, Electric field control of the magnetic chiralities in ferroaxial multiferroic RbFe (MoO₄)₂. *Physical review letters* **108**, 237201 (2012).
12. J. Yang *et al.*, Electric - Field Manipulation of Magnetic Chirality in a Homo - Ferro - Rotational Helimagnet. *Advanced Science* **11**, 2402048 (2024).
13. S. Hayami, Ferroaxial moment induced by vortex spin texture. *Physical Review B* **106**, 144402 (2022).
14. T. Nagai, Y. Mochizuki, S. Yoshida, T. Kimura, Chemical Aspect of Displacive-Type Ferroaxial Phase Transition from Perspective of Second-Order Jahn–Teller Effect: NASICON Systems as an Example. *Journal of the American Chemical Society* **145**, 8090-8098 (2023).
15. T. Nagai, T. Kimura, Chemical Switching of Ferroaxial and Nonferroaxial Structures Based on Second-Order Jahn–Teller Activity in (Na, K) 2Hf (BO₃)₂. *Chemistry of Materials* **35**, 4109-4115 (2023).
16. Y. Kajita, T. Nagai, S. Yamagishi, K. Kimura, M. Hagihala, T. Kimura, Ferroaxial transitions in glaserite-type Na₂BaM (PO₄)₂ (M= Mg, Mn, Co, and Ni). *Chemistry of Materials* **36**, 7451-7458 (2024).
17. J. Yang, F.-T. Huang, S.-W. Cheong, Unlocking magnetic ferro-rotational functionalities. *Journal of Physics: Condensed Matter* **37**, 195801 (2025).
18. Y. Kajita, T. Hayashida, S. Yamagishi, K. Kimura, T. Kimura, Ferroaxial Domain Imaging in Glaserite-type Na₂Ba M (PO₄)₂ (M= Mn, Co, and Ni). *Journal of the Physical Society of Japan* **94**, 063702 (2025).
19. T. Hayashida *et al.*, Visualization of ferroaxial domains in an order-disorder type ferroaxial crystal. *Nature communications* **11**, 1-8 (2020).
20. T. Hayashida *et al.*, Phase transition and domain formation in ferroaxial crystals. *Physical Review Materials* **5**, 124409 (2021).
21. H. Yokota, T. Hayashida, D. Kitahara, T. Kimura, Three-dimensional imaging of ferroaxial domains using circularly polarized second harmonic generation microscopy. *npj Quantum Materials* **7**, 1-6 (2022).
22. X. Guo *et al.*, Ferrorotational domain walls revealed by electric quadrupole second harmonic generation microscopy. *Physical Review B* **107**, L180102 (2023).

23. B. B. Van Aken, J.-P. Rivera, H. Schmid, M. Fiebig, Observation of ferrotoroidic domains. *Nature* **449**, 702-705 (2007).
24. A. Waśkowska, L. Gerward, J. S. Olsen, W. Morgenroth, M. Mączka, K. Hermanowicz, Temperature- and pressure-dependent lattice behaviour of RbFe (MoO₄)₂. *Journal of Physics: Condensed Matter* **22**, 055406 (2010).
25. W. Jin *et al.*, Observation of a ferro-rotational order coupled with second-order nonlinear optical fields. *Nature Physics* **16**, 42-46 (2020).
26. R. Owen *et al.*, Second-order nonlinear optical and linear ultraviolet-visible absorption properties of the type-II multiferroic candidates RbFe (A O₄)₂ (A= Mo, Se, S). *Physical Review B* **103**, 054104 (2021).
27. M. Fiebig, D. Fröhlich, B. Krichevstov, R. V. Pisarev, Second harmonic generation and magnetic-dipole-electric-dipole interference in antiferromagnetic Cr₂O₃. *Physical Review Letters* **73**, 2127 (1994).
28. M. Fiebig, D. Fröhlich, G. Sluyterman v. L, R. Pisarev, Domain topography of antiferromagnetic Cr₂O₃ by second - harmonic generation. *Applied Physics Letters* **66**, 2906-2908 (1995).
29. S.-W. Cheong, S. Lim, K. Du, F.-T. Huang, Permutable SOS (symmetry operational similarity). *npj Quantum Materials* **6**, 1-10 (2021).
30. J. Hlinka, J. Privratska, P. Ondrejko, V. Janovec, Symmetry guide to ferroaxial transitions. *Physical review letters* **116**, 177602 (2016).
31. S.-W. Cheong, D. Talbayev, V. Kiryukhin, A. Saxena, Broken symmetries, non-reciprocity, and multiferroicity. *npj Quantum Materials* **3**, 1-7 (2018).
32. G. Liu *et al.*, Electrical switching of ferro-rotational order in nanometre-thick 1T-TaS₂ crystals. *Nature Nanotechnology*, 1-7 (2023).
33. K.-i. Uchida, J. P. Heremans, Thermoelectrics: From longitudinal to transverse. *Joule* **6**, 2240-2245 (2022).
34. A. Hunter *et al.*, Non-Fermi liquid quasiparticles in strain-tuned Sr₂RuO₄. *arXiv preprint arXiv:2503.11311*, (2025).
35. M. Först *et al.*, Nonlinear phononics as an ultrafast route to lattice control. *Nature Physics* **7**, 854-856 (2011).
36. D. Fausti *et al.*, Light-induced superconductivity in a stripe-ordered cuprate. *science* **331**, 189-191 (2011).
37. R. Mankowsky *et al.*, Nonlinear lattice dynamics as a basis for enhanced superconductivity in YBa₂Cu₃O₆. *Nature* **516**, 71-73 (2014).
38. R. Mankowsky, A. von Hoegen, M. Först, A. Cavalleri, Ultrafast reversal of the ferroelectric polarization. *Physical review letters* **118**, 197601 (2017).
39. D. M. Juraschek, M. Fechner, N. A. Spaldin, Ultrafast structure switching through nonlinear phononics. *Physical review letters* **118**, 054101 (2017).
40. P. G. Radaelli, Breaking symmetry with light: Ultrafast ferroelectricity and magnetism from three-phonon coupling. *Physical Review B* **97**, 085145 (2018).
41. T. Nova, A. Disa, M. Fechner, A. Cavalleri, Metastable ferroelectricity in optically strained SrTiO₃. *Science* **364**, 1075-1079 (2019).
42. X. Li *et al.*, Terahertz field-induced ferroelectricity in quantum paraelectric SrTiO₃. *Science* **364**, 1079-1082 (2019).
43. A. S. Disa *et al.*, Polarizing an antiferromagnet by optical engineering of the crystal field. *Nature Physics* **16**, 937-941 (2020).
44. A. Stupakiewicz *et al.*, Ultrafast phononic switching of magnetization. *Nature Physics* **17**, 489-492 (2021).
45. A. S. Disa, T. F. Nova, A. Cavalleri, Engineering crystal structures with light. *Nature Physics* **17**, 1087-1092 (2021).
46. Z. Zeng *et al.*, Photo-induced chirality in a nonchiral crystal. *Science* **387**, 431-436 (2025).

47. D. A. Bustamante Lopez, D. M. Juraschek, M. Fechner, X. Xu, S.-W. Cheong, W. Hu, Ultrafast simultaneous manipulation of multiple ferroic orders through nonlinear phonon excitation. *npj Quantum Materials* **10**, 24 (2025).
48. H. Ueda *et al.*, Tuning chirality amplitude at ultrafast timescales. *arXiv preprint arXiv:2504.07599*, (2025).
49. D. Afanasiev *et al.*, Ultrafast control of magnetic interactions via light-driven phonons. *Nature Materials* **20**, 607-611 (2021).
50. D. M. Juraschek, M. Fechner, A. V. Balatsky, N. A. Spaldin, Dynamical multiferroicity. *Physical Review Materials* **1**, 014401 (2017).
51. D. M. Juraschek, P. Narang, N. A. Spaldin, Phono-magnetic analogs to opto-magnetic effects. *Physical Review Research* **2**, 043035 (2020).
52. D. M. Juraschek, T. Neuman, P. Narang, Giant effective magnetic fields from optically driven chiral phonons in 4 f paramagnets. *Physical Review Research* **4**, 013129 (2022).
53. J. Luo *et al.*, Large effective magnetic fields from chiral phonons in rare-earth halides. *Science* **382**, 698-702 (2023).
54. M. Basini *et al.*, Terahertz electric-field driven dynamical multiferroicity in SrTiO₃ *Nature* **628**, 534-539 (2024).
55. C. Davies, F. Fennema, A. Tsukamoto, I. Razdolski, A. Kimel, A. Kirilyuk, Phononic switching of magnetization by the ultrafast Barnett effect. *Nature* **628**, 540-544 (2024).
56. T. Kahana, D. A. Bustamante Lopez, D. M. Juraschek, Light-induced magnetization from magnonic rectification. *Science Advances* **10**, eado0722 (2024).
57. Z. He, G. Khalsa, Optical control of ferroaxial order. *Physical Review Research* **6**, 043220 (2024).
58. M. E. Lines, A. M. Glass, *Principles and applications of ferroelectrics and related materials*. (Oxford university press, 2001).
59. C. Kittel, P. McEuen, *Introduction to solid state physics*. (John Wiley & Sons, 2018).
60. Y. Wang *et al.*, Axial Higgs mode detected by quantum pathway interference in RTe₃. *Nature* **606**, 896-901 (2022).
61. Y. Kajita, T. Nagai, S. Yamagishi, K. Kimura, M. Hagihala, T. Kimura, Ferroaxial Transitions in Glaserite-Type Na₂BaM (PO₄)₂ (M= Mg, Mn, Co, and Ni). *Chemistry of Materials*, (2024).
62. J. Yang, F.-T. Huang, S.-W. Cheong, Unlocking magnetic ferro-rotational functionalities. *Journal of Physics: Condensed Matter*, (2025).
63. M. Henstridge, M. Först, E. Rowe, M. Fechner, A. Cavalleri, Nonlocal nonlinear phononics. *Nature Physics* **18**, 457-461 (2022).
64. V. A. Abalmasov, Ultrafast reversal of the ferroelectric polarization by a midinfrared pulse. *Physical Review B* **101**, 014102 (2020).
65. A. S. Zimmermann, D. Meier, M. Fiebig, Ferroic nature of magnetic toroidal order. *Nature communications* **5**, 4796 (2014).
66. S. Hayami, R. Oiwa, H. Kusunose, Electric ferro-axial moment as nanometric rotator and source of longitudinal spin current. *Journal of the Physical Society of Japan* **91**, 113702 (2022).
67. S. Hayami, R. Oiwa, H. Kusunose, Unconventional Hall effect and magnetoresistance induced by metallic ferroaxial ordering. *Physical Review B* **108**, 085124 (2023).
68. J. Hohlfeld, T. Gerrits, M. Bilderbeek, T. Rasing, H. Awano, N. Ohta, Fast magnetization reversal of GdFeCo induced by femtosecond laser pulses. *Physical Review B* **65**, 012413 (2001).
69. A. Kimel, A. Kirilyuk, P. Usachev, R. Pisarev, A. Balbashov, T. Rasing, Ultrafast non-thermal control of magnetization by instantaneous photomagnetic pulses. *Nature* **435**, 655-657 (2005).
70. C. D. Stanciu *et al.*, All-optical magnetic recording with circularly polarized light. *Physical review letters* **99**, 047601 (2007).

71. K. Vahaplar *et al.*, All-optical magnetization reversal by circularly polarized laser pulses: Experiment and multiscale modeling. *Physical Review B—Condensed Matter and Materials Physics* **85**, 104402 (2012).
72. A. Khorsand *et al.*, Role of magnetic circular dichroism in all-optical magnetic recording. *Physical review letters* **108**, 127205 (2012).
73. A. Stupakiewicz, K. Szerenos, D. Afanasiev, A. Kirilyuk, A. Kimel, Ultrafast nonthermal photo-magnetic recording in a transparent medium. *Nature* **542**, 71-74 (2017).
74. A. V. Kimel, M. Li, Writing magnetic memory with ultrashort light pulses. *Nature Reviews Materials* **4**, 189-200 (2019).
75. A. Sell, A. Leitenstorfer, R. Huber, Phase-locked generation and field-resolved detection of widely tunable terahertz pulses with amplitudes exceeding 100 MV/cm. *Optics letters* **33**, 2767-2769 (2008).
76. Z. H. Amber, B. Kirbus, L. M. Eng, M. Rüsing, Quantifying the coherent interaction length of second-harmonic microscopy in lithium niobate confined nanostructures. *Journal of Applied Physics* **130**, (2021).
77. A. Barker Jr, Temperature Dependence of the Transverse and Longitudinal Optic Mode Frequencies and Charges in SrTi O 3 and BaTi O 3. *Physical Review* **145**, 391 (1966).
78. G. Kresse, J. Hafner, Ab initio molecular dynamics for liquid metals. *Physical review B* **47**, 558 (1993).
79. G. Kresse, J. Furthmüller, Efficiency of ab-initio total energy calculations for metals and semiconductors using a plane-wave basis set. *Computational materials science* **6**, 15-50 (1996).
80. G. Kresse, J. Furthmüller, Efficient iterative schemes for ab initio total-energy calculations using a plane-wave basis set. *Physical review B* **54**, 11169 (1996).
81. A. Togo, First-principles phonon calculations with phonopy and phono3py. *Journal of the Physical Society of Japan* **92**, 012001 (2023).
82. G. Kresse, D. Joubert, From ultrasoft pseudopotentials to the projector augmented-wave method. *Physical review b* **59**, 1758 (1999).
83. H. J. Monkhorst, J. D. Pack, Special points for Brillouin-zone integrations. *Physical review B* **13**, 5188 (1976).
84. S. Klimin *et al.*, Structural phase transition in the two-dimensional triangular lattice antiferromagnet RbFe (MoO 4) 2. *Physical Review B* **68**, 174408 (2003).